2006

Image-based Nanocrystallography with Online Database Support

Peter Moeck
Portland State University, pmoeck@pdx.edu

Ján Zahornadsky
Charles University of Prague

Boris Dusek
Charles University of Prague

Citation Details

Peter Moeck ; Ján Zahornadský ; Boris Dušek and Philip Fraundorf, "Image-based nanocrystallography with online database support", Proc. SPIE 6370, Nanomaterial Synthesis and Integration for Sensors, Electronics, Photonics, and Electro-Optics, 63701A (October 19, 2006); doi:10.1117/12.676656; http://dx.doi.org/10.1117/12.676656

Image-based Nanocrystallography with on-line Database Support

Peter Moeck[1,Ω], Ján Zahornadský[1,2], Boris Dušek[1,2], and Philip Fraundorf[3]

[1] Nanocrystallography Group, Department of Physics, Portland State University, P.O. Box 751, Portland, OR 97207-0751, USA; [Ω] Oregon Nanoscience and Microtechnologies Institute, http://www.onami.us

[2] Faculty of Mathematics and Physics, Charles University of Prague, Ke Karlovu 3, 12116 Praha, The Czech Republic

[3] Department of Physics and Astronomy and Center for Molecular Electronics, University of Missouri at St. Louis, MO 53121, USA

ABSTRACT

The crystallographic phase and morphology of many materials change with the crystal size so that new needs arise to determine the crystallography of nanocrystals. Direct space high-resolution phase-contrast transmission electron microscopy (HRTEM) and atomic resolution scanning TEM (STEM) when combined with tools for image-based nanocrystallography in two (2D) and three (3D) dimensions possess the capacity to meet these needs. After a concise discussion of lattice-fringe visibility spheres and maps, this paper discusses lattice-fringe fingerprinting in 2D and tilt protocol applications. On-line database developments at Portland State University (PSU) that support image-based nanocrystallography are also mentioned.

Keywords: crystallography, nanocrystals, HRTEM and STEM images, lattice fringes, crystallographic databases

1. INTRODUCTION

Recent nanotech developments create new needs for the characterization of nanocrystals. Conventional (parallel illumination) transmission electron microscopy (TEM) and scanning probe TEM (STEM) traditionally provide structural, chemical, and morphological information of crystalline materials. Medium acceleration voltage (200 - 400 kV) high-resolution TEMs (HRTEMs [1] and STEMs [2] without aberration correctors) provide 2D projections of the 3D electrostatic potential energy distribution within crystals with a directly interpretable spatial resolution in the range of approximately 0.2 - 0.136 nm*.

Due to the tiny size of nanocrystals, some well established electron crystallography characterization methods that are based on dynamic electron scattering effects such as convergent beam electron diffraction (CBED) cannot satisfy the above mentioned needs. This is because (medium acceleration voltage) CBED disks are largely devoid of their fine structure [3] when the nanocrystal diameter is on the order of 10 nm.

In the first part of this paper, the concepts of lattice-fringe visibility spheres and maps are discussed. In the second part of this paper, we briefly review lattice-fringe fingerprinting in two dimensions (i.e. on the basis of 2D projections without tilting the nanocrystals). On-line database developments at Portland State University (PSU) are mentioned. There developments are for both the community of electron microscopists (that work with inorganic materials) and the community of materials science educators. Tilt protocol applications are reviewed as supporting methods for analyzing crystalline nanoparticles in 3D in the third part of this paper. Sub-stoichiometric Tungsten Carbide and Tungsten nanocrystals as well as Altaite/Clausthalite nano-islands are chosen as examples.

For both conceptual and practical reasons, we restrict the application of our image-based nanocrystallography tools to the point resolution of the microscope. Note that the viability of image-based nanocrystallography in either 2D or 3D improves super-linearly with the microscope's point resolution [4,5]. The word "fringe" is typically used in physics for any periodic light or dark band produced by diffraction or interference of electromagnetic or matter waves. We use the words "lattice fringes" here for periodic contrast variations in HRTEM or STEM images.

Nanomaterial Synthesis and Integration for Sensors, Electronics, Photonics, and Electro-Optics, edited by Nibir K. Dhar, Achyut K. Dutta, M. Saif Islam, Proceedings of SPIE Vol. 6370, 63701A, (2006) · 0277-786X/06/$15 · doi: 10.1117/12.676656

2. LATTICE-FRINGE VISIBILITY SPHERES AND MAPS

A kinematical theory of lattice-fringe visibility in HRTEM has recently been developed by P. Fraundorf and co-workers [6-8]. The heuristic value of this theory is founded in the remarkable fact that one of its model representations, the lattice-fringe visibility map, is in a sense the direct space equivalent of the well known (computer generated) Kikuchi diffraction** map [9]. There are, however, important differences between these two types of maps.

Lattice-fringe visibility maps only contain crystallographic planes that are occupied by atoms, while Kikuchi diffraction maps contain up to instrumental (i.e. small diffraction angles) and attenuation limits the multiples (n) of allowed net planes (according to $n \cdot \lambda = 2d_{hkl} \sin\Theta = 2d_{HKL} \sin\Theta$, with $n \cdot h = H$, etc.). The widths of the crystallographic bands in lattice-fringe visibility maps are directly proportional to the crystallographic plane spacings and indirectly proportional to the wavelength of the transmitted electrons (i.e. directly proportional to the acceleration voltage that acts on the electron beam). These direct space proportionalities are reciprocal to those that apply to (reciprocal space) Kikuchi maps.

Following a kinematical approach, ideal (zero-dimensional) reciprocal lattice points (corresponding to an infinitely large crystal) are expanded in a first approximation into reciprocal lattice spheres, Fig. 1, as a result of small size effects of spherical nanoparticles. A perfectly symmetric intersection of two corresponding reciprocal lattice spheres for ($\pm\vec{g}$) with the Ewald sphere would result in lattice fringes becoming visible over two symmetrically equivalent cones of incident electron-beam directions, Fig. 2.

From the intersection of the spherical range of reciprocal space around the tip of $+\vec{g}$ with the Ewald sphere, a cone of incident electron beam directions results that contains $\vec{k}_o$, i.e. the vector from A to O, as its axis, and also comprises all other incident directions that fulfill the Laue condition. The angular width of this cone that is associated with $+\vec{g}$ is the angle BOC, which is also one half of the nanocrystal tilt-range over which crystallographic planes ($\pm\vec{g}$ bands, Friedel pairs) are (reliably) visible in a real HRTEM image (if their direct-space net-plane spacings are larger than the point resolution of the microscope).

Note that the second reciprocal lattice sphere that is associated with $-\vec{g}$ would intersect the Ewald sphere when $\vec{k}_o$ and $-\vec{g}$ make an angle $\leq 90° + \text{BOC}$. This would lead to a second cone of incident electron-beam directions of exactly the same size as the first cone and in mirror symmetric orientation with respect to this cone.

The angular width of the BOC cone of incident electron-beam directions is proportional to the width of the corresponding crystallographic band in a direct-space model sphere that represent a nanocrystal with a spherical shape, Fig. 3. We call these direct-space spheres with overlaid visible fringes simply lattice-fringe visibility spheres, Fig. 3.

Since nanocrystals possess certain symmetries, their lattice-fringe visibility spheres have to show the same symmetries. Systematic absences due to non-primitive (higher symmetric) choices of the unit cell are also revealed in fringe-visibility spheres. In Fig. 3, i.e. the lattice-fringe visibility sphere of gold nanocrystals, space group $Fm\bar{3}m$, there are for example no {100} fringes visible since the face centering of the conventional non-primitive unit cell results in lattice points (and atoms) residing at unit cell positions of ½ 0 0, 0 ½ 0, and 0 0 ½.

Since HRTEM structure images are the result of interferences of several diffracted beams with the transmitted beam (but ideally not of interferences with each other, i.e. linear imaging), the other rules of systematic absences (which are due to the presence of screw-axis and glide-plane symmetry elements) apply also to lattice-fringe visibility spheres. In addition, only those crystallographic planes will be visible which actually contain atoms and whose spacing can be resolved with a given electron microscope at the Scherzer resolution.

In short, the kinematic theory of lattice-fringe visibility, Figs. 1-3, describes how crystallographic bands (net planes with appropriate direct-space spacings) become visible on (3D) lattice-fringe visibility spheres. Lattice-fringe visibility maps, on the other hand, are simply the (2D) stereographic projections of the corresponding lattice-fringe visibility spheres or of sections of these spheres, Figs. 4a,b. Note that the stereographic projection [10] preserves the angles between crystallographic planes (i.e. interfringe angles) and, therefore, the angles between zone axes are also preserved.

When lattice-fringe visibility maps are properly calibrated, experimental HRTEM images can be directly compared and indexed with these maps, just as Kikuchi diffraction patterns can be compared with simulated Kikuchi maps in order to index such patterns. The more details a lattice-fringe visibility map contains, e.g. Fig. 4b for a prospective point resolution of 0.06 nm, the more useful it will be in comparing to experimental HRTEM images.

Due to their relationship with reciprocal lattice spheres, the widths of the crystallographic bands in lattice-fringe visibility spheres and maps are inversely proportional to the size of the nanocrystal. For HRTEM images from smaller nanocrystals, this means that the same crystallographic planes are visible over a wider range of incident electron beam

directions. Both lattice-fringe visibility maps and Kikuchi maps can be used analogously as "road maps" to guide the tilting of crystals in a TEM.

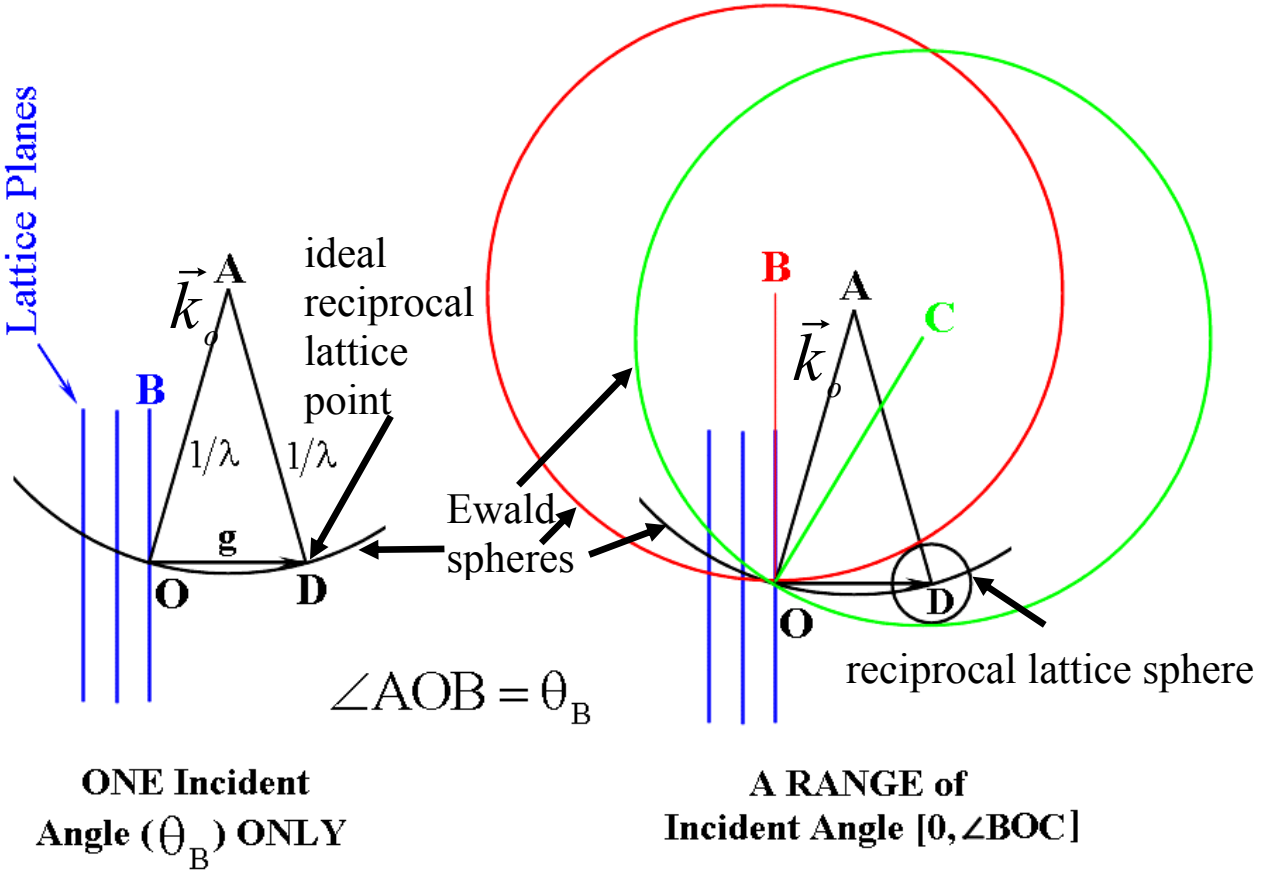

Fig. 1: (left) Sketch to show a reciprocal lattice sphere due to small size effects of nanocrystals and how its existence leads to a cone of primary electron-beam directions that fulfills the Laue condition. Ideal reciprocal lattice points (left) that the kinematical diffraction theory predicts for infinitely large crystals are expanded into reciprocal lattice spheres for nanocrystals **(right)**. An ideal reciprocal lattice point intersects the Ewald sphere in just one mathematical point which is defined by the Laue equation $\vec{k} - \vec{k}_o = \vec{g} + \vec{s}$ with $\vec{s} = \vec{0}$ (left). A reciprocal lattice sphere, on the other hand, intersects the Ewald sphere over a range in reciprocal space since the Laue equation $\vec{k} - \vec{k}_o = \vec{g} + \vec{s}$ can be fulfilled for a sphere of radius $\vec{s} \neq \vec{0}$ (right). (Modified after a sketch from Wentao Qin.)

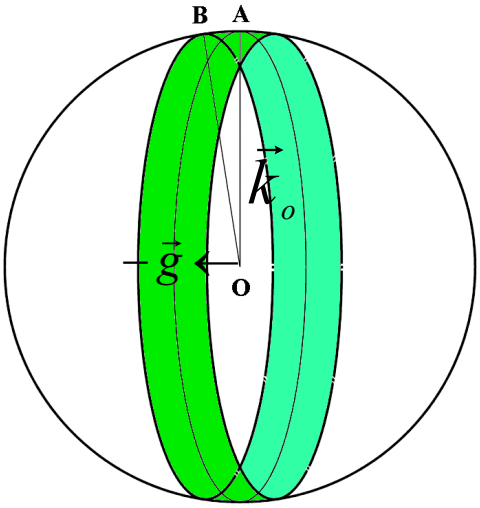

Fig. 2: Sketch to show how the two cones of incident electron-beam directions (two shaded areas) that are mirror symmetric about the central crystallographic net plane (which contains all rotation-symmetric primary beam vectors $\vec{k}_o$ that are perpendicular to the normal to this plane) result in two fringes (one for each sign of $\pm\vec{g}$ also called a Friedel pair) becoming visible on a model direct-space sphere (lattice-fringe visibility sphere). The radius of this sphere is conveniently chosen to be proportional to the radius of the nanoparticle which it represents in the context of lattice-fringe visibility spheres. The widths of fringes on a lattice-fringe visibility sphere are directly proportional to their corresponding reciprocal lattice spheres (Fig. 1 right) and are chosen to be proportional to their corresponding direct-space net-plane spacings. (Modified after a sketch from Wentao Qin).

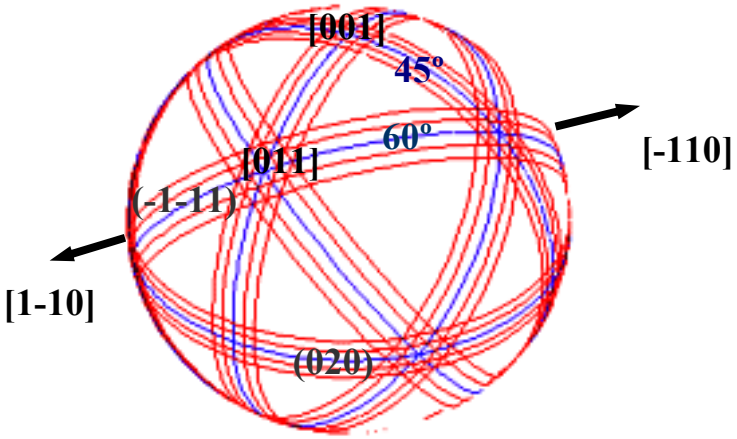

Fig. 3: Lattice-fringe visibility sphere for gold nanocrystals, point resolution 0.19 nm. Fringes that are visible at this resolution are indexed; the crossings of such fringes reveal visible zone axes. The lattice-fringe visibility bands are divided into 4 stripes, so that the symmetry of the zone axes becomes apparent.

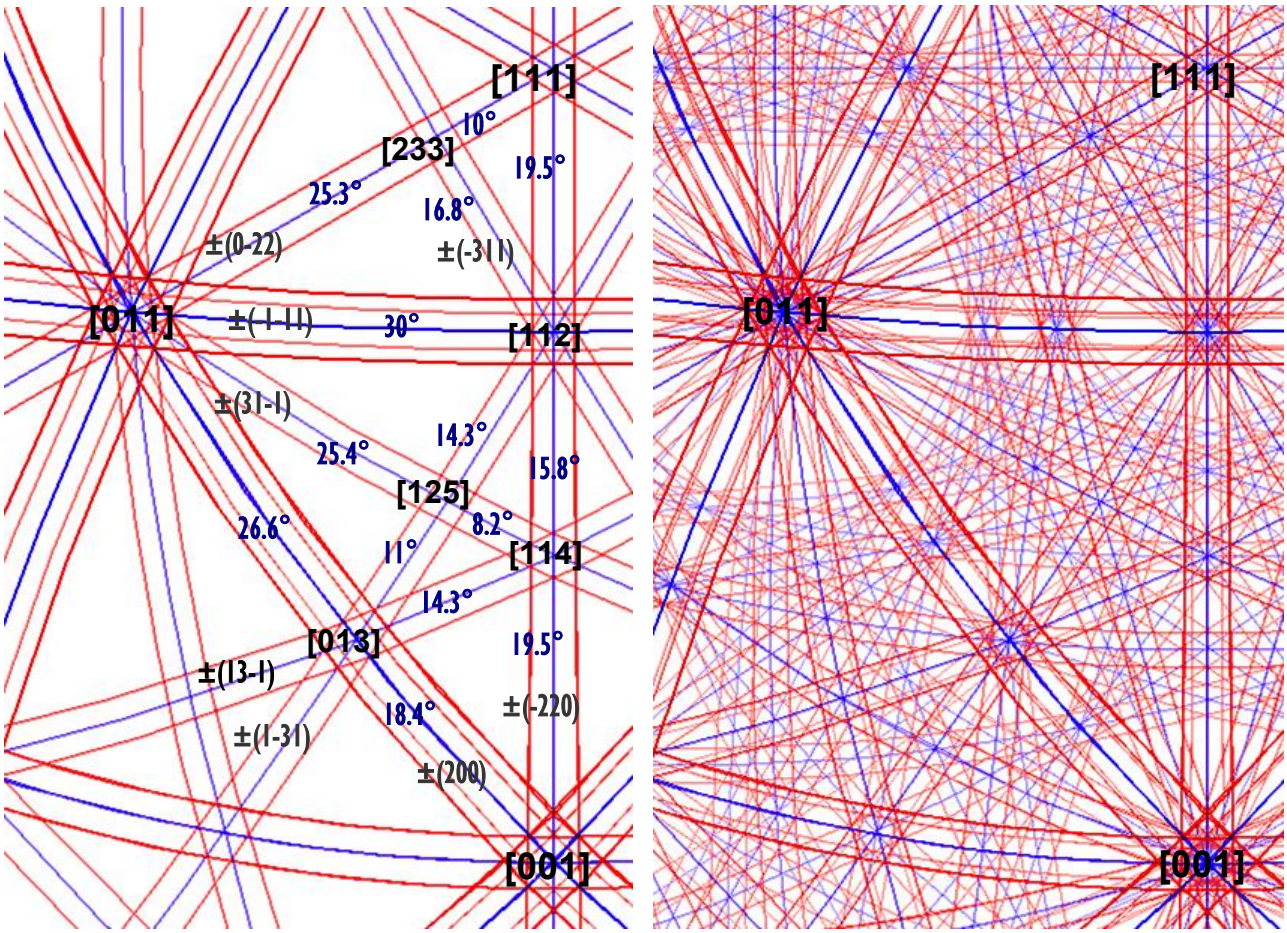

Fig. 4: (a) Lattice-fringe visibility map for gold, point resolution 0.12 nm (as obtainable with e.g. a C_s-corrected FEI Tecnai G^2 F20 ST microscope at 200 kV or a JEOL JEM-ARM1250 microscope at 1250 kV). Visible fringes and their zone axis intersections are labeled. The angles between zone axes are given; **(b)** Lattice-fringe visibility map for gold, point resolution 0.06 nm (as prospectively obtainable with 300 kV aberration corrected "TEAM project [11]" microscopes). The four widest lattice fringe visibility bands are divided into 4 stripes, so that the symmetry of the zone axes becomes apparent.

As mentioned in the introduction, the crystallographic information that can be harnessed by the tools described in this paper increases with improvements in directly interpretable image resolution. This effect is demonstrated by the lattice-fringe visibility maps of gold, Figs. 4a and 4b. Note that the computer generated lattice-fringe visibility map of gold for a point resolution of 0.06 nm, Fig. 4b, looks rather similar to a computer generated Kikuchi map of gold. Since a similar amount of crystallographic information is encoded in high resolution lattice-fringe visibility maps and Kikuchi maps, much of the crystallography that has traditionally been derived from Kikuchi diffraction patterns can be obtained from images that are recorded in aberration-corrected TEMs and STEMs.

3. LATTICE-FRINGE FINGERPRINTING IN TWO DIMENSIONS

As a high-resolution conceptual extension to certain aspects of fluctuation or variable coherence microscopy [12,13], lattice-fringe fingerprinting was recently proposed by P. Fraundorf and co-workers. Lattice-fringe fingerprint plots [14-16], represent in their most basic form a plot of visible interfringe angles of crossed fringes versus the respective reciprocal lattice spacings of these fringes. Figure 5 shows, for example, theoretical lattice-fringe fingerprint plots for ensembles of the two titania phases Rutile and Brookite in their most basic form (and in the kinematical diffraction limit) for a typical point resolution of a non-aberration corrected HRTEM. (As mentioned above, the criterion for a lattice fringe being visible here is that its spatial frequency is reliably transferred to the HRTEM or STEM image.)

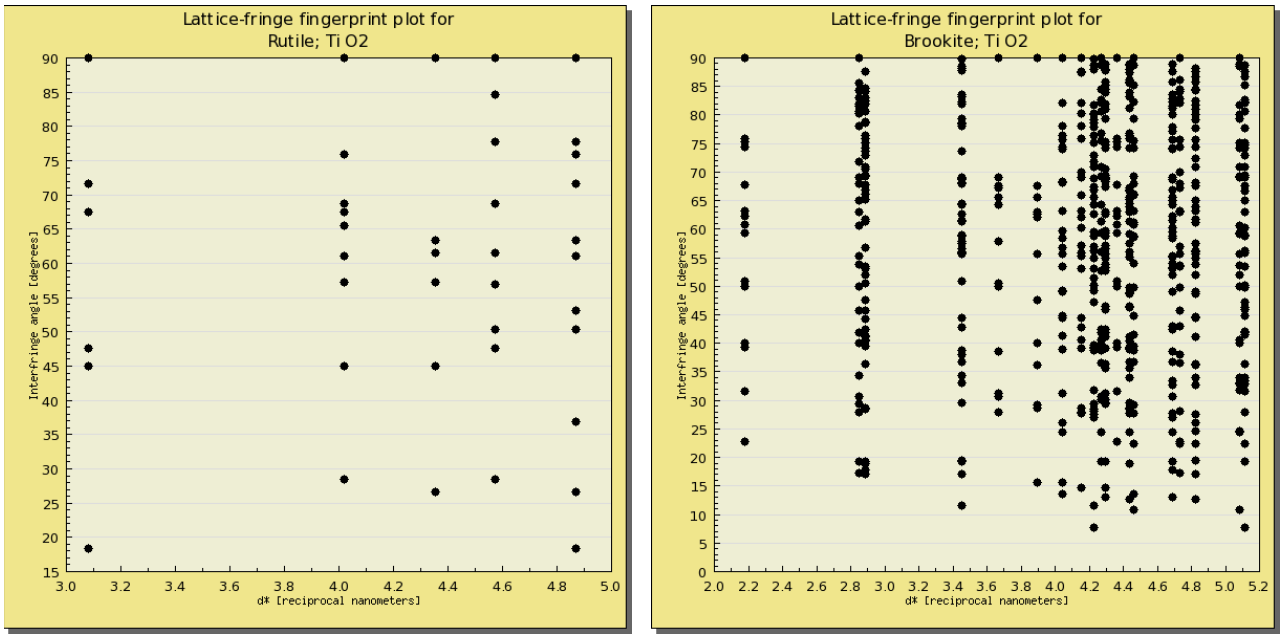

Fig. 5: Basic theoretical lattice-fringe fingerprint plots for two titania polymorphs **(left) Rutile** and **(right) Brookite** in the kinematical diffraction limit for a microscope point resolution of 0.19 nm. Although the stoichiometry of both titania phases is identical, the lattice-fringe fingerprint plots look rather different, i.e. characteristic of the individual polymorphs. (The crystallographic data for both polymorphs are given in the appendix in a format that is endorsed by the International Union of Crystallography.)

The utility of such theoretical lattice-fringe fingerprint plots, e.g. Fig. 5, is founded in them being a rather specific characteristic for an ensemble of nanocrystals against which experimental data from HRTEM (or STEM [17]) images can be directly compared for the identification of unknown nanocrystal phases. When compared to powder diffraction pattern, which may alternatively be called "diffraction fingerprints", lattice-fringe fingerprint plots contain (in the same spatial frequency range) much more crystal specific information for the unique identification of nanocrystals.
In addition, the crystal phase characteristics of lattice-fringe fingerprint plots can be determined with a high accuracy and precision. The net-plane spacings that correspond to lattice fringes can, for example, be determined experimentally from digitally recorded images [18-20] with a statistical precision of 0.0001 to 0.005 nm in dependence of specimen characteristics such as the electron dose and the size of the measured area. For the angles of intersecting lattice-fringes,

the corresponding statistical precisions range from 0.1° to 0.5°. A slow-scan charge coupled device (CCD) camera with 1024 times 1024 pixels at a magnification of 250,000 was employed in those studies [20] and CCD cameras with more pixels are supposed to lead to even better precisions.

Under favourable experimental conditions (uniform areas of equal thickness and without visible defects) as well as an internal calibration such as a known crystalline material near the specimen area of interest, lattice-fringe spacings can be measured with an accuracy of better than a few ten-thousands of a nanometer and the angles of intersecting lattice-fringes can be obtained with errors smaller than 0.1° [20]. Under less favourable experimental conditions (thickness variations and defects) and a typical external calibration of the microscope's magnification, these systematic errors are likely to be one order of magnitude larger [18]. One can, nevertheless, be quite confident that local variations of the lattice parameters for regions as small as 1.5 to 0.8 nm in diameter can be measured [18,20]. (Additional measurement errors are likely to occur for theoretical reasons if two lattice fringes with almost the same orientation and very close spacing are present in an image [19]. This latter situation is, however, practically rather rare.)

Summarized the above briefly, there is additional crystal phase specific information to be gained from the analyses of lattice fringes and that information can be extracted with high accuracies and precisions. This makes the identification of unknowns by lattice-fringe fingerprinting in a TEM competitive to the well established "powder X-ray diffraction fingerprinting" methods.

W. J. de Ruijter et al. concluded already in 1995 that because *"lattice-fringe vector measurements for identification of unknown materials ... must still be compared manually with X-ray diffraction databases ..."* it would be beneficial "*to establish an automated link with these databases and associated search/matching programs thus enabling immediate printout of a list of possible materials and phase names.*" [20]. A multi-year project that addresses these concerns was started 10 years later by the Nanocrystallography Group of PSU [15,16,21-23].

For a start, we provide a *free* on-line crystallography database that supports both the communities of electron microscopists (that work with inorganic materials) and of materials science educators. At our project's website [23] and on the basis of our **critically evaluated** (syntax and semantics corrected) mainly inorganic subset of the Crystallography Open Database [24], we provide computer access to approximately 10,000 reports on full structure determinations, i.e. lattice parameters, space group, atomic coordinates, and bibliographic reference. The left side of Figure 6 shows, for example, a shot of the search screen for the titania phase Brookite. The results of this search are given in the right side of Fig. 6. (Clicking on the items CIF view or download will result in access to the full structure determination report in a standardized file format that is endorsed by the International Union of Crystallography. Abbreviated examples of two such files are given in the appendix.)

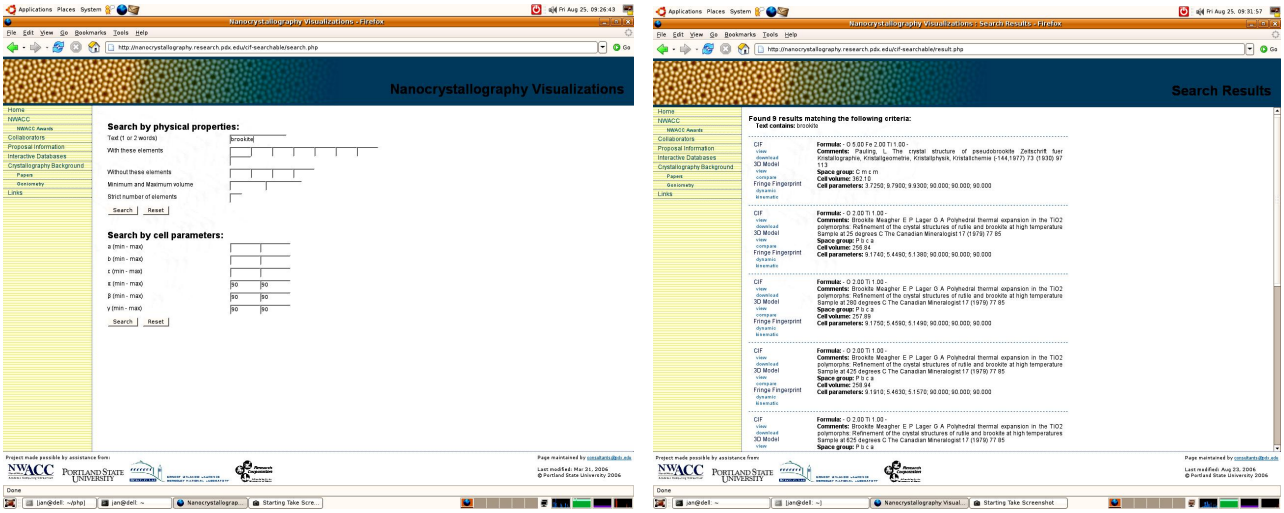

Fig. 6: Search of our mainly inorganic subset [23] of the Crystallography Open Database [24]; **(left)** Screenshot of the search screen for the titania phase Brookite; **(right)** Screenshot of the search results (currently 13 entries including pseudo-brookite and rutile).

To support lattice-fringe fingerprinting in 2D, we currently provide on our project web site [23] the options to calculate and display basic lattice-fringe fingerprint plots in both the kinematic and dynamic diffraction limits, e.g., compare Figs. 5 and 7. The dynamic diffraction limit is taking account of double and multiple diffraction within a single nanocrystal. Our project web site [23] can also be used to display and compare structures (CIFs), e.g. Fig. 8.

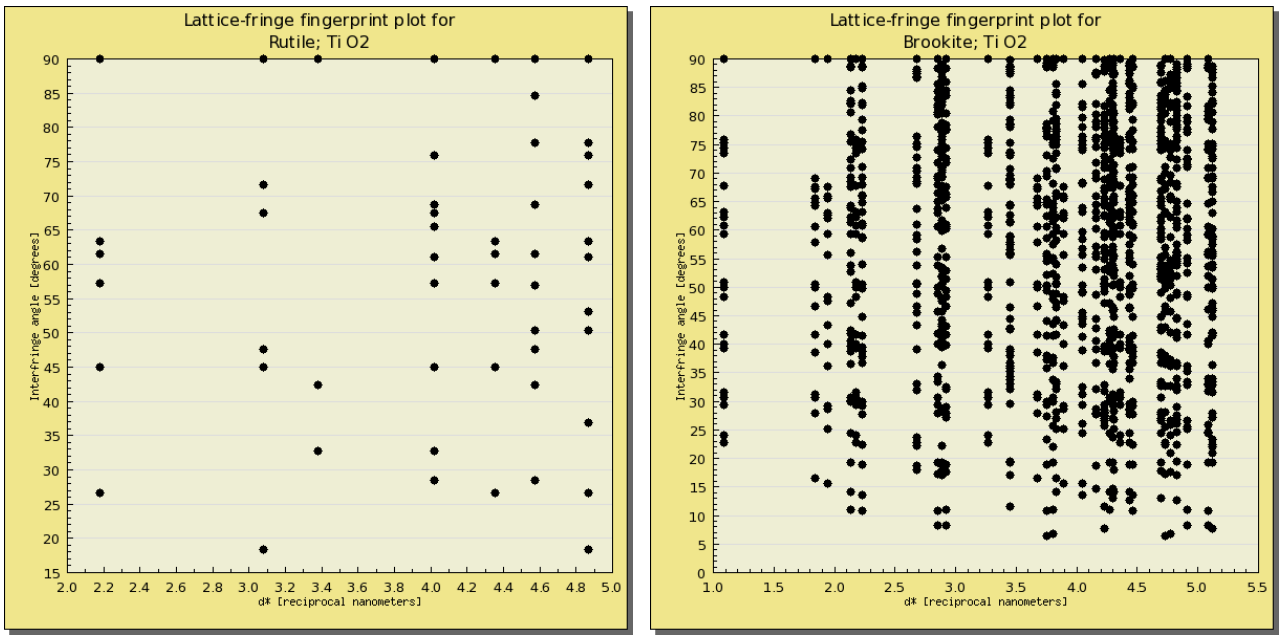

Fig. 7: Basic theoretical lattice-fringe fingerprint plots for the two titania polymorphs **(left) Rutile** and **(right) Brookite** in the dynamical diffraction limit for a microscope point resolution of 0.19 nm.

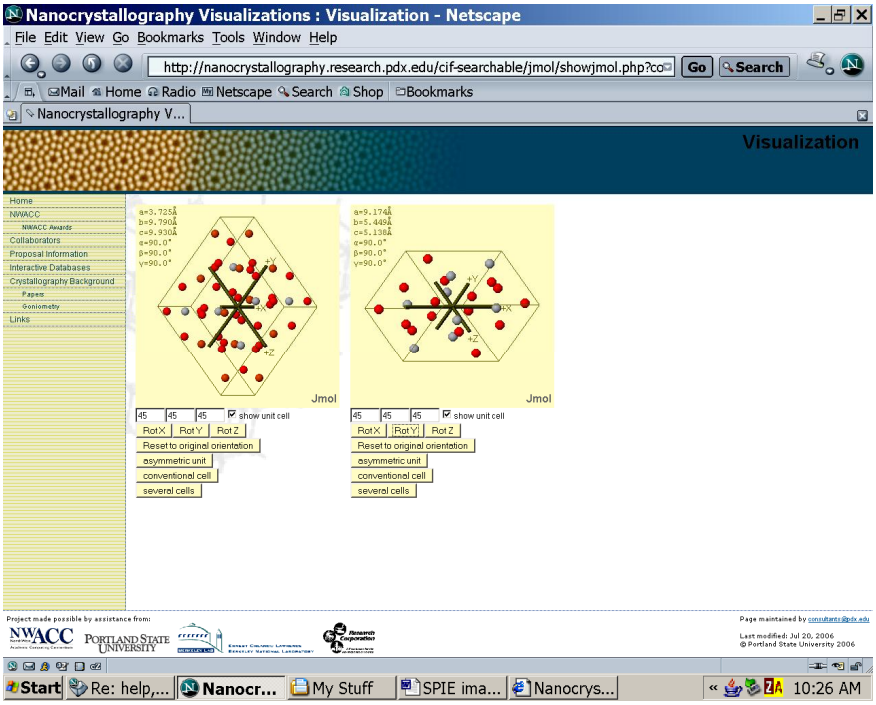

Fig. 8: Screenshot from our project's website [23] which compares the unit cells of **Pseudo-brookite**, Fe_2O_5Ti, **(left)** and **Brookit**e, TiO_2, **(right)**. The 2D projections are orthographic, i.e. the observer's eyes are assumed to be perpendicular to the computer screen. The crystal structure orientations can be changed interactively and independently of each other, providing "quasi-3D visualizations".

Because lattice-fringe fingerprinting in 2D with on-line database support is amendable to automation, we will start automation of the whole procedure in 2007. The Oregon Nanoscience and Microtechnologies Institute will support these developments since they have commercial potential.

4. TILT PROTOCOL APPLICATIONS

Tilt protocol applications are discussed by P. Fraundorf and co-workers in refs. [6,7,25,26] and Moeck et al. [5,27,28]. The applications of such protocols are special cases of the more general transmission electron goniometry [5,28] since the latter delivers the transformation matrix between the crystallographic coordinate system of the crystal under investigation and the Cartesian coordinate system of the electron microscope. This matrix and its derivatives serve as the basis for many kinds of crystallographic analyses. Tilt protocol applications, on the other hand, do not require the determination of this matrix. Only the crystallographic tilt and its tilt axis are important for tilt protocol applications, but not the actual goniometer settings before and after the tilt. These sets of goniometer settings are, on the other hand, crucial experimental data for transmission electron goniometry.

Figure 9 summarizes a range of tilt protocols for face-centered cubic and body-centered cubic nanocrystals that can be realized with non-aberration corrected HRTEMs and STEMs. Tilt protocols may be divided into three groups, *(i)* minimalistic protocols that deliver the minimal data set for deriving lattice parameters in 3D [26], *(ii)* two-zone axis protocols including tests for symmetry elements, and *(iii)* advanced tilt protocols consisting of more than one crystallographic tilt. When the point resolution is sufficiently high, a zone axis may be revealed by the crossing of more than two fringes, e.g. Figs. 4a,b. (Since Fig. 9 was designed to show tilt protocols that can be employed in non-aberration corrected HRTEM and STEM with a point resolution in the range of 0.2 to 0.15 nm for crystals with small lattice constants, no two zone-axis tilt protocols where the zone axis are revealed by more than two crossing fringes is shown in this figure.)

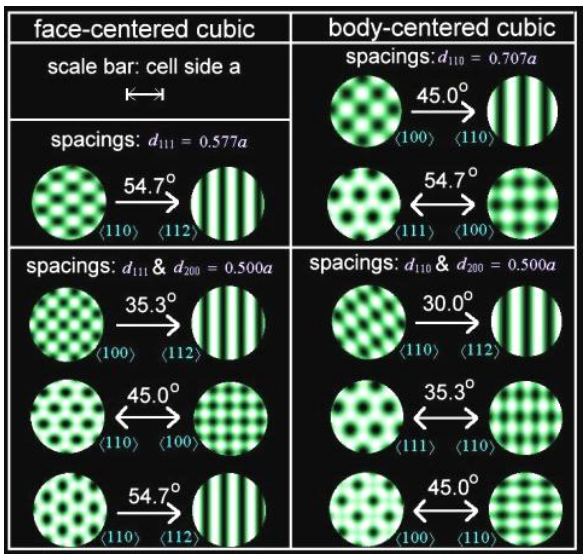

Fig. 9: Chart of tilt protocols for face-centered cubic and body-centered cubic nanocrystals with small lattice constants (i.e. metals and other densely packed materials such as ceramics with one large and one small atom per lattice point) that can be applied in non-aberration corrected HRTEMs and STEMs with point resolutions in the range 0.2 to 0.15 nm.

Minimalistic tilt protocols encompass at least three non-coplanar reciprocal lattice vectors, one zone axis that is revealed by crossed fringes and one zone axis that is inferred from the orientation of a fringe with respect to the tilt axis and tilt angle. Figure 9 gives 5 such tilt protocols. In the following, the face-center cubic minimalistic <100> → <112> tilt protocol, as given in the left column and second row of Fig. 9, is discussed.

An ensemble of randomly oriented sub-stoichiometric WC_{1-x} particles with the halite structure (2-x atoms at a lattice point) serves as experimental example. The tilt protocol was performed in an HRTEM that possesses a point resolution of 0.19 nm and was equipped with a double-tilt goniometer that allows for ± 15 ° (α_{max}) tilt around the eucentric axis of the side entry rod and ± 10° (β_{max}) tilt perpendicular to this axis [7,26]. Since the WC_{1-x} nanocrystals possess a lattice constant of 0.425 nm, only {200} and {111} fringes are resolved in the respective HRTEM images. For the halite structural prototype, crossed {200} fringes result in <001> zone axes being visible, crossed {111} fringes result in <011> zone axes being visible. While the smallest tilt angle between <001> and <011> zone axes is 45°, the smallest tilt angle between two different <011> zones is 60°, see Fig. 3. The maximum combined tilt of the goniometer is, however,

only 35.5° (i.e. arc cos (cos $2\alpha_{max} \cdot \cos 2\beta_{max}$). Two-zone axis protocols can, therefore, not be employed.
From Fig. 9 we can infer that an anti-clockwise tilt of 35.3° around [-110] (i.e. the cross product of [001] and [112]) will result in a nanocrystal that was aligned parallel to [001] before the application of the tilt protocol becoming aligned parallel to [112] after the application of the tilt protocol. This example of a tilt protocol application delivered the basis for both the determination of the lattice constant of WC_{1-x} nanocrystals and the identification of their phase out of 35 candidate structures [7,26].
Two zone-axis protocols encompass at least four non-coplanar reciprocal lattice vectors and two zone axes that are revealed by crossed fringes. Fig. 9 gives four such tilt protocols. To illustrate a two zone-axis protocol and information given in the right column of Fig. 9 for body-centred cubic crystals, the following example deals with Tungsten nanocrystals. Like most body-centred cubic lattices, space group $Im\bar{3}m$, with one atom at a lattice point, tungsten possesses a rather small lattice constant: 0.3165 nm. A point resolution of 0.15 nm is therefore required to reveal <011> zone axes by the crossings of {200} and {110} fringes and <111> zone axes by crosses of symmetrically equivalent {110} fringes. The two-zone axis tilt protocol becomes, therefore, [111] → [110], left column, forth row in Fig. 9, were the tilt axis is [-110] and the tilt angle is 35.3° (anticlockwise).
Another example of a two-zone axis tilt protocol application to a face-centered cubic crystal with the halite structure is given in ref. [27]. Altaite/Clausthalite nano-islands on (001) oriented clausthalite substrate were tilted from [111] to [112] in order to confirm pseudomorph heteroepitaxial growth, Fig. 10. Since the semiconductor Clausthalite possesses the rather large lattice constant of 0.625 nm, {111}, {200} and {220} fringes are revealed already in a microscope with a point resolution of 0.22 nm. The <111> zone axes are, thus, revealed by crossing {220} fringes and the <112> zone axes are revealed by crosses of {220} and {111} fringes. The relative small tilt of 19.5° anticlockwise around the [1-10] axis is then sufficient to tilt from [111] to [112]. As nanocrystals with rather large lattice constants were involved, this tilt protocol is not shown schematically in Fig. 10.

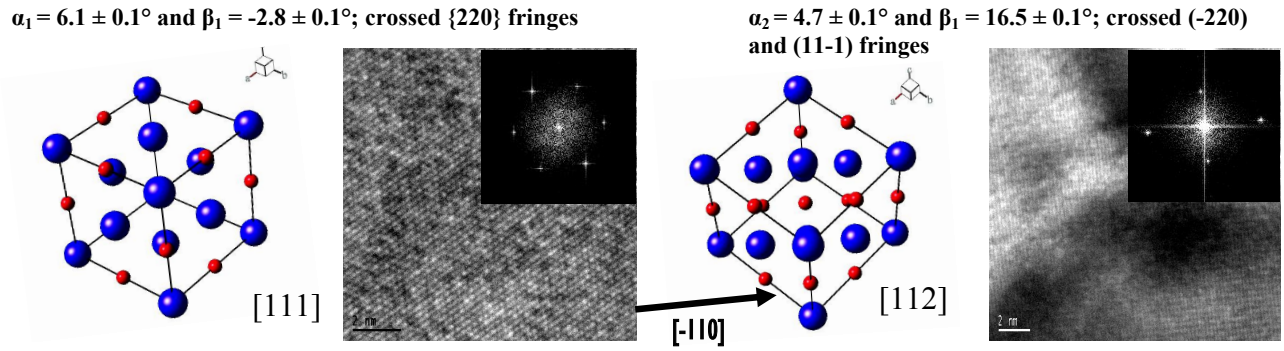

Fig. 10: Sketch of the face-center cubic minimalistic [111] → [112] tilt protocol for nanocrystals with the halite (rock salt) structure, rotating the crystal anticlockwise 19.5° around [-110]. Corresponding HRTEM images of the **Clausthalite (left)** substrate and **Altaite/Clausthalite nano-islands (right).** The contrast variations across the right image are due to pseudomorphic lattice-mismatch strain between the nano-islands and the substrate. Note the different magnifications. (The sketches of the halite structure in [111] and [112] orientation were created with the shareware program "Balls & Sticks", Version 1.52, 2004, by S. J. Kang and T. C. Ozawa, see http://www.softbug.com/toycrate/bs for *free* downloads. The unit cell is displayed in the perspective projection mode, so that atoms do not exactly fall on top of each other in a 2D projection. 3D anaglyph glasses may be used in connection with this visualization program.)

Increased point resolution, Figs. 4a,b, will enable more advanced tilt protocols that consist of more than one crystallographic tilt. Between the 8 visible zone axes in one stereographic [001]-[011]-[111] triangle (which represents $^1/_{24}$ of the orientation half space and can by the application of the symmetry elements of the space group $Fm\bar{3}m$ cover the whole orientation space) that are indexed in Figs. 4a.b, there are no less than 28 (= $8 \cdot {}^7/_2$) possible two-zone axis tilt protocols to employ. Out of these 28 two-zone axis tilt protocols, there are three that test for the simultaneous existence of symmetry axes at both zone axes, i.e. [001] → [011], [001] → [111], and [011] → [111]. The testing for the existence of projected symmetry elements for the identification of a nanocrystal phase, thus, emerges as a potential application of tilt protocols in HRTEMs and STEMs with a sufficiently high point resolution.
Figure 11 shows, for example, the two possible cases of orientations of three different symmetry axes in a cube. The combined presence or absence of such symmetry axes in a cubic nanocrystal can be determined by the application of three subsequent two-axis tilt protocols. Nanocrystals with point groups 23 or m3, on the one hand, and 432, $\bar{4}3m$, or

m$\bar{3}$m, on the other hand, can be distinguished from the presence of either a two fold or a four fold axis parallel to <100>. Fig. 12 finally illustrates how PSU's nanocrystallography visualization website may be used to support the application of tilt protocols.

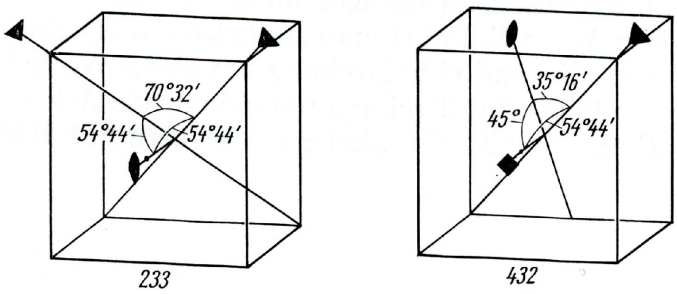

Fig. 11: Sketch of the two possible combinations of three different symmetry axes in a cube (from ref. [29]). The application of three subsequent two-zone axis tilt protocols allows for a distinction between subgroups of the cubic point symmetry group a nanocrystal may belong to.

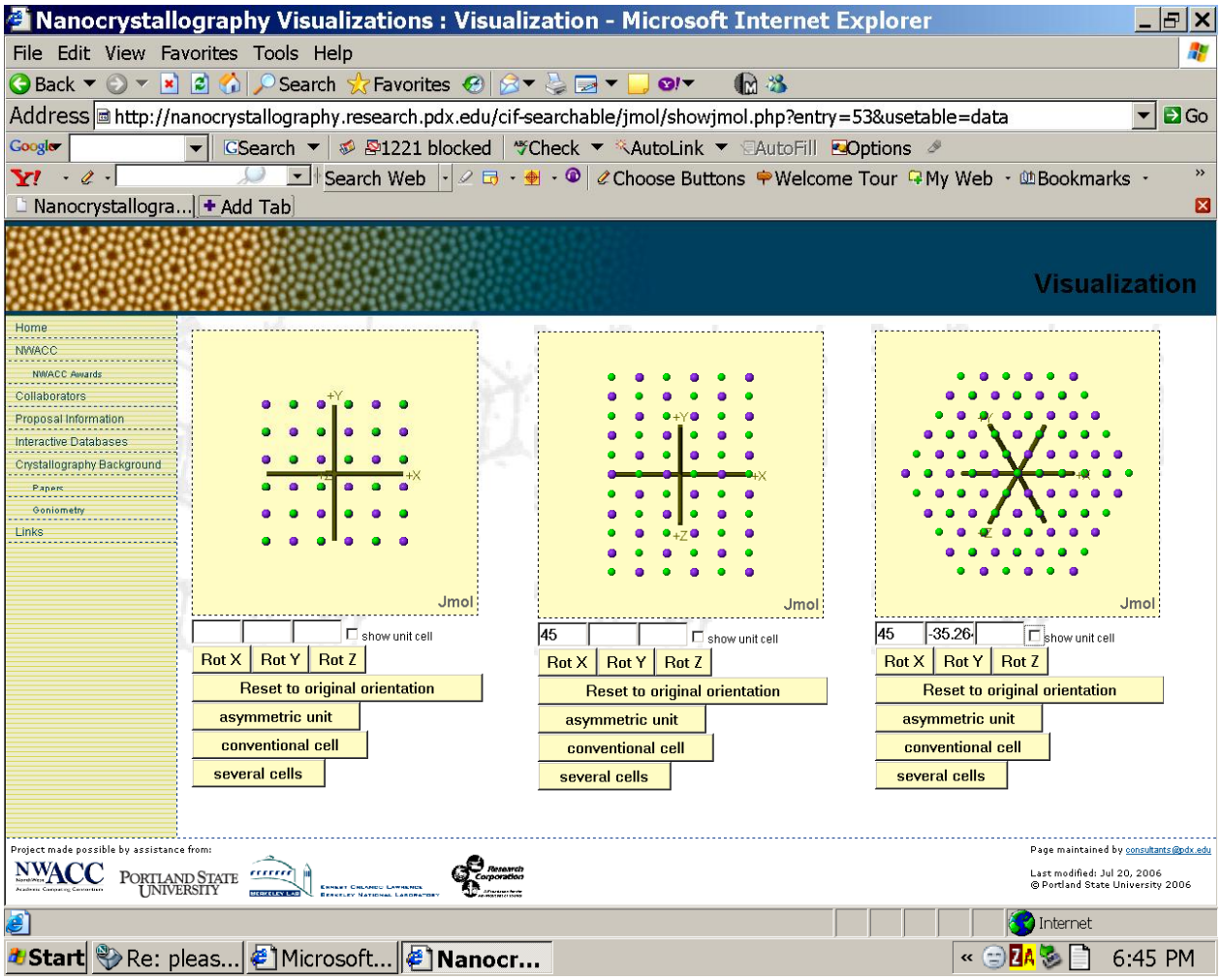

Fig. 12: Screenshot composite of quasi-3D visualizations of the halite structure: **(left)** [001] projection – default and original orientation, **(middle)** [011] projection (one 45° anti-clockwise rotation around [100]), and **(right)** [111] projection (one additional 35.264° clockwise rotation around [010]. Such rather large tilts should be possible in aberration-corrected TEMs even in an eucentric mode [30] since there can be much more free space around the specimen in such microscopes. The 2D projections are orthographic.

SUMMARY AND CONCLUSIONS

After a concise introduction to lattice-fringe visibility spheres and maps, this paper discussed lattice-fringe fingerprinting in 2D and (3D) tilt protocol applications. On-line database developments at Portland State University that support image-based nanocrystallography were also mentioned. Because lattice-fringe fingerprinting in 2D with on-line database support is amendable to automation, we will start a corresponding project in 2007. This can be considered as a realization of W. J. de Ruijter's and co-workers' concluding remarks of their 1995 paper.

ACKNOWLEDGMENTS

This research was supported by an award from Research Corporation. Additional support was provided by PSU in the form of faculty enhancement, faculty development, and internationalization awards. Dr. Bjoern Seipel from PSU's Nanocrystallography Group is thanked for providing the halite structure sketches in Fig. 10 and for working on the program for the calculation of kinematic lattice-fringe fingerprint plots. William Garrick from PSU's Academic and Research Computing is thanked for his continuous interest and for managing the research servers that host our database.

REFERENCES

1. D.J. Smith, "The realization of atomic resolution with the electron microscope", *Rep. Prog. Phys.* **60**, 1513-1580 (1997).
2. N.D. Browning et al., "Atomic Resolution Scanning Transmission Electron Microscopy", *phys. stat. sol. (b)* **227**, 229-245 (2001).
3. D.B. Williams and C.B. Carter, *Transmission electron microscopy: a textbook for materials science,* Plenum Press, New York, 1996.
4. P. Moeck, W. Qin, and P.B. Fraundorf, "Image-based nanocrystallography in future aberration corrected transmission electron microscopes", *Mat. Res. Soc. Symp. Proc.* Vol. **818**, M11.3.1-M11.3.6 (2004).
5. P. Moeck, W. Qin, and P.B. Fraundorf, "Image-based nanocrystallography by means of transmission electron goniometry", *Nonlinear Analysis* **63**, e1323-e1331 (2005).
6. P. Fraundorf et al., "Making sense of nanocrystal lattice fringes", *J. Appl. Phys*. **98**, 114308-1-114308-10 (2005); *arXiv:cond- mat/0212281 v2*.
7. W. Qin, *Direct space (nano)crystallography via high-resolution Transmission Electron Microscopy*, PhD thesis**,** University of Missouri-Rolla, (2000).
8. P. Fraundorf and W. Qin, "Fringe Visibility Maps", *Microsc. Microanal.* **7**(Suppl. 2), 272-273 (1999).
9. J.L. Bomback and L.E. Thomas, "Generation and Applications of Computer Drawn Kikuchi Maps", *J. Appl. Cryst.* **4**, 356-370 (1971).
10. O. Johari and G. Thomas, *The stereographic projection and its application*, Wiley, 1969.
11. U. Dahmen, "The TEAM Project – An Update", *Microsc. Microanal.* **11**(Suppl 2), 2142-2143 (2005).
12. M.M.J. Tracy and J.M. Gibson, "Variable coherence microscopy: a rich source of structural information from disordered systems", *Acta Cryst.* **A 52**, 212-220 (1996).
13. P.M. Voyles. J.M. Gibson, and M.M.J. Tracy, "Fluctuation microscopy: A probe of atomic correlations in disordered materials", *J. Electron. Microsc.* **49**, 259-266 (2000).
14. P. Fraundorf et al., "Fringe-covariance "fingerprinting" of nanoparticle lattice images", *Microsc. Microanal.* **10** (Suppl 2), 1262-1263 (2004).
15. P. Moeck et al., "Identifying unknown nanocrystals by fringe fingerprinting in two dimensions & free-access crystallographic databases", *Proc. of SPIE*, Vol. **6000**, 60000M-1 – 60000M-12 (2005).
16. P. Moeck et al., "Lattice fringe fingerprinting in two dimensions with database support", *NSTI-Nanotech 2006,* Vol. **1**, 741-744 (2006) *(ISBN 0-9767985-6-5)*.
17. P. Wang et al., "Geometric aspects of lattice contrast visibility in nanocrystalline materials using HAADF STEM, *Ultramicroscopy* **106**, 277-283 (2006).
18. W.J. de Ruijter et al., "Quantification of high-resolution lattice images and electron holograms", *Scanning Microscopy* (Suppl. **6**), 347-359 (1992).
19. W.J. de Ruijter, "Measurement of Lattice-Fringe Vectors from Digital HREM Images: Theory and Simulations", *J.*

Computer-Aided Microscopy **6**(4), 195-212 (1994).
20. W.J. de Ruijter et al., "Measurement of lattice-fringe vectors from digital HREM images: experimental precision", *Ultramicroscopy* **57**, 409-422 (1995).
21. P. Moeck et al., "Crystal structure visualizations in three dimensions with support from the open access Nano-Crystallography Database", *J. Mater. Educ.* **28**(1), 87-95 (2006).
22. P. Moeck et al., "Freely Accessible Internet Resources for Nanoscience and Nanotechnology Education and Research at Portland State University's Research Servers", *Mat. Res. Soc. Symp. Proc.* Vol. **931**, 0931-KK01-04 (2006).
23. http://nanocrystallography.research.pdx.edu
24. M. Leslie (editor), "Free the Crystals", *Science* **310**, 597 (2005).
25. P. Fraundorf, "Determining the 3D Lattice Parameters of Nanometer-sized Single Crystals from Images", *Ultramicroscopy* **22**, 225-230 (1987).
26. W. Qin and P. Fraundorf, "Lattice parameters from direct-space images at two tilts", *Ultramicroscopy* **94**,245-262 (2003); *arXiv:cond-mat/0001139.*
27. P. Moeck et al., "Nominal PbSe nano-islands on PbTe: grown by MBE, analyzed by AFM and TEM", *Mat. Res. Soc. Symp. Proc.* Vol. **829**, B9.4.1-B9.4.6 (2005).
28. P. Moeck, W. Qin, and P. Fraundorf, "Towards 3D image-based nanocrystallography by means of transmission electron goniometry", *Mat. Res. Soc. Symp. Proc.* Vol. **839**, P4.3.1-P4.3.6 (2005).
29. W. Kleber, *Einführung in die Kristallographie*, 17th ed., Verlag Technik Berlin, 1990.
30. U. Valdré and K. Tsuno, "A Contribution to the Unsolved Problem of a High-Tilt Fully Eucentric Goniometer Stage", *Acta Cryst. A* **44**, 775-780 (1988).

* Silicon crystals in the <110> orientation showing two 0.136 nm spaced atoms that appear as "dumbbells" in this projection typically serve to demonstrate the respective point resolution of high resolution transmission electron microscopes.

** Kikuchi diffraction lines and bands support controlled tilting of crystals in a TEM since their projected movements appear on the TEM's screen as quasi-straight lines that are rigidly fixed to the crystals.

APPENDIX

```
_chemical_name_common 'Rutile'
loop_
_publ_author_name
'Meagher E P'
'Lager G A'
_journal_name_full "The Canadian Mineralogist"
_journal_volume 17
_journal_year 1979
_journal_page_first 77
_journal_page_last 85
_publ_section_title
;
 Polyhedral thermal expansion in the TiO2 polymorphs: Refinement of the crystal
structure of rutile and brookite at high temperature Sample at 25 degrees C
;
_chemical_formula_sum 'Ti O2'
_cell_length_a 4.593
_cell_length_b 4.593
_cell_length_c 2.959
_cell_angle_alpha 90
_cell_angle_beta 90
_cell_angle_gamma 90
_symmetry_space_group_name_H-M 'P 42/m n m'
_space_group.reference_setting '136:-P 4n 2n'
loop_
_atom_site_label
_atom_site_fract_x
_atom_site_fract_y
_atom_site_fract_z
_atom_site_U_iso_or_equiv
Ti  0.00000  0.00000  0.00000  0.00532
O  0.30510  0.30510  0.00000  0.00760
```

```
_chemical_name_common 'Brookite'
loop_
_publ_author_name
'Meagher E P'
'Lager G A'
_journal_name_full "The Canadian Mineralogist"
_journal_volume 17
_journal_year 1979
_journal_page_first 77
_journal_page_last 85
_publ_section_title
;
 Polyhedral thermal expansion in the TiO2 polymorphs: Refinement of the crystal
structures of rutile and brookite at high temperature Sample at 25 degrees C
;
_chemical_formula_sum 'Ti O2'
_cell_length_a 9.174
_cell_length_b 5.449
_cell_length_c 5.138
_cell_angle_alpha 90
_cell_angle_beta 90
_cell_angle_gamma 90
_symmetry_space_group_name_H-M 'P b c a'
_space_group.reference_setting '061:-P 2ac 2ab'
loop_
_atom_site_label
_atom_site_fract_x
_atom_site_fract_y
_atom_site_fract_z
Ti  0.12890  0.09720  0.86280
O1  0.00950  0.14910  0.18350
O2  0.23140  0.11100  0.53660
```

Note that the unit-cell lengths are given in Å; that the unit-cell angles are given in degrees; that the (unambiguous space group symmetry and origin choice) notations of the "Symmetry CIF Dictionary", Version 1.0.1 of June 17, 2005, http://www.iucr.org/, are given; and that the symmetry equivalent positions are omitted for brevity.